

## Article

# Trifluoromethyl Substituted Derivatives of Pyrazoles as Materials for Photovoltaic and Electroluminescent Applications

Monika Pokladko-Kowar <sup>1,\*</sup>, Ewa Gondek <sup>1,\*</sup>, Andrzej Danel <sup>1</sup>, Tomasz Uchacz <sup>2</sup>, Paweł Szlachcic <sup>3</sup>, Katarzyna Wojtasik <sup>1,\*</sup>  and Paweł Karasiński <sup>4</sup> 

<sup>1</sup> Department of Physics, Cracow University of Technology, Podchorążych Str. 1, 30-084 Krakow, Poland; rrdanela@cyf-kr.edu.pl

<sup>2</sup> Faculty of Chemistry, Jagiellonian University, Gronostajowa Str. 2, 30-387 Krakow, Poland; uchacz@chemia.uj.edu.pl

<sup>3</sup> Faculty of Food Technology, Agricultural University, Balicka Str. 122, 31-149 Krakow, Poland; pawel.szlachcic@urk.edu.pl

<sup>4</sup> Department of Optoelectronics, Silesian University of Technology, B. Krzywoustego 2, 44-100 Gliwice, Poland; pawel.karasinski@polsl.pl

\* Correspondence: mpokladkokowar@pk.edu.pl (M.P.-K.); egondek@pk.edu.pl (E.G.); katarzyna.wojtasik@pk.edu.pl (K.W.)

**Abstract:** New 6-CF<sub>3</sub>-1*H*-pyrazolo[3,4-*b*]quinolines with a methyl and/or phenyl group attached to the pyrazole core (Molx (*x* = 1, 2, 3, 4)) were synthesized and characterized in terms of their optoelectronic applications: photovoltaic and electroluminescence. The fluorescence emissions of the investigated phenyl-decorated pyrazoloquinolines is caused by the photoinduced charge transfer *p* process occurring between the phenyl substituent and the pyrazoloquinoline core, while 1,3-dimethyl-6-CF<sub>3</sub>-1*H*-pyrazolo[3,4-*b*]quinoline exhibits an  $\pi,\pi^*$ -type emission. The number of phenyls and their substitution positions modulate both emission properties and HOMO energy levels. Next, the bulk heterojunction BHJ solar cells based on 1*H*-pyrazolo[3,4-*b*]quinoline derivatives with architecture ITO/PEDOT:PSS/PDT + Molx/Al were fabricated. The organic active layer was a blend of Molx and poly(3-decylthiophene-2,5-diyl). The complex refractive index and the layer thickness of the organic solar cells were determined using a spectroscopic ellipsometer Woollam M2000 (J.A. Woollam Co., Inc., Lincoln, NE, USA) and CompleteEASE software. For solar devices with the best value of power efficiency of approximately 0.38%, the thickness of the active layer (Mol3 + PDT) was 111 nm, with a short-circuit current density of  $J_{SC} = 32.81 \mu\text{A}/\text{cm}^2$  and an open-circuit voltage of  $V_{OC} = 0.78 \text{ V}$ . Finally, we demonstrated double-layer light-emitting diodes with an organic active layer (Molx + PVK) and an electron transporting material layer, ETM (2-[3,5-bis(4-phenyl-2-quinolyl)phenyl]-4-phenylquinoline (Tris-Q). Bright bluish-green light originating from the active layer was observed in the double-layer device, ITO/PEDOT:PSS/active layer/ETM/Ca/A. The active layer was a mixture of PV-doped 1*H*-pyrazolo[3, 4-*b*]quinoline dyes. An OLED device was constructed by employing Molx as an emitter, which gave a deep bluish-green emission with the spectra range of 481–506 nm. The best value of the maximum brightness at approximately 1436.0 cd/m<sup>2</sup> was achieved for a diode based on Mol3 (1-phenyl-3-phenyl-6-CF<sub>3</sub>-1*H*-pyrazolo[3,4-*b*]quinoline) and [R<sup>1</sup> = Ph, R<sup>3</sup> = Ph and R<sup>6</sup> = CF<sub>3</sub>]. The current efficiency was up to 1.26 cd/A at 506 nm with a CIE of 0.007, 0.692.

**Keywords:** solar cells; photovoltaic cells; PV; 1*H*-pyrazolo[3,4-*b*]quinoline; electroluminescence; OLED



**Citation:** Pokladko-Kowar, M.; Gondek, E.; Danel, A.; Uchacz, T.; Szlachcic, P.; Wojtasik, K.; Karasiński, P. Trifluoromethyl Substituted Derivatives of Pyrazoles as Materials for Photovoltaic and Electroluminescent Applications. *Crystals* **2022**, *12*, 434. <https://doi.org/10.3390/cryst12030434>

Academic Editor: Saripally Sudhaker Reddy

Received: 24 February 2022

Accepted: 15 March 2022

Published: 21 March 2022

**Publisher's Note:** MDPI stays neutral with regard to jurisdictional claims in published maps and institutional affiliations.



**Copyright:** © 2022 by the authors. Licensee MDPI, Basel, Switzerland. This article is an open access article distributed under the terms and conditions of the Creative Commons Attribution (CC BY) license (<https://creativecommons.org/licenses/by/4.0/>).

## 1. Introduction

In recent decades, we have seen significant progress in research into the use of organic materials such as polymers, copolymers, oligomers and small molecule compounds in organic optoelectronics such as organic photovoltaic devices [1], organic transistors [2], organic light emitting diodes (OLEDs) [3], sensors [4] and batteries [5]. Based on the

achievements to date in the field of organic electronics, it can be assumed that in the future they may completely displace their inorganic counterparts. The main advantages of organic materials are low production costs, ease of structural modification, the possibility of application on large surfaces and the possibility of printing on flexible substrates. One of the disadvantages is the lower mechanical or chemical resistance compared to inorganic materials [6,7]. There are three types of photovoltaic device: (i) inorganic photovoltaic cells (such as crystalline-silicon (c-Si) solar cells or amorphous silicon (*a*-Si), CdTe and CuInGaSe<sub>2</sub> (CIGS), etc.) [8], (ii) plastic photovoltaic cells, and (iii) hybrid photovoltaic cells (such as “inorganics-in-organics” or superiorities of hybrid perovskite) [8–10]. Plastic photovoltaic devices include organic solar cells based on small molecular compounds, polymer or copolymers, dye sensitized solar cells (DSSCs) and tandem cells [8,11]. The organic bulk heterojunction (BJH) photovoltaic cells are one of the architectures of organic solar cells. Other structures of organic solar cells are organic single-layer solar cells, bi-layer (*p*-*n* junction) solar cells, inverted solar cells and tandem solar cells. The active layer of the BJH solar cell architecture most often uses conjugated polymers [10,12] as donors and different types of acceptors such as fullerene derivatives [13,14], small molecular compounds [15] and nanoparticles [16]. In 1995, Heeger et al. [17] first invented and described the structure of an organic photovoltaic cell with a BJH layer as the active layer. The active layer was a mixture of poly(2-methoxy-5-(2-ethylhexyloxy)-1,4-phenylenevinylene) (MEH-PPV) and 1-(3-methoxycarbonyl)propyl-1-phenyl [6,6]C<sub>61</sub> (PCBM), where MEH-PPV was the donor and PCBM was the acceptor [17–19]. The best conversion efficiency PCE for BHJ organic photovoltaic (OSCs) devices was, at that time, approximately 13.1%. In these investigated devices, the active layer was a blend of donor and acceptor materials, where the donor was a new polymer (PBDB-T-SF) and the acceptor was a new small molecule (IT-4F) [20]. In 2018, Hang Yin et al. [21] presented the results for bulk heterojunction devices with a binary active layer PCDTBT:PC71BM, and they achieved a power conversion efficiency of 16.5% and 20.8% for a structure with a ternary BHJ cell of PCDTBT:PDTSTPD:PC71BM. For solar cells based on GaAs thin film, the best world conversion efficiencies were 27.6% [22], approximately 22% for bulk single crystal Si [23] and 20% for perovskite solar cells [24], 14% for dye-sensitized cells [25] and 11.1% for organic solar cells [26]. In addition to organic photovoltaics, there is also a rapidly developing field of organic electroluminescence. Since the first electroluminescence in organic materials based on anthracene single crystals, reported in 1965, there has been a rapid development of research in this direction that embraces the electroluminescence of organic materials [27]. However, the significant breakthrough came over twenty years later when Tang and VanSlyke constructed a two-layer electroluminescent cell using an aromatic amine as a hole-transporting layer and a complex of aluminium and 8-hydroxyquinoline AlQ<sub>3</sub> serving as the light emitting and electron transporting layer. Luminance exceeded 1000 cd/m<sup>2</sup> below 10 V, with a quantum efficiency of 1% photon/electron being achieved. Their pioneering work [28] initiated further OLED research based on small molecules and polymers [29,30]. The first OLED based on a polymer was reported in 1990 by Friend et al. [31]. In recent decades, the attention on organic light-emitting diodes has increased significantly due to their advantages, such as their high flexibility [32,33], as well as the fact they are lightweight and super thin [34], cost and power efficient, environment friendly [35,36] and have high luminous efficiency and great colour contrast [37,38]. In 2002, Mao and et al. produced the three-layered EL device with the structure ITO/CuPc/DPPPhP/BDCM/Mg:Ag, where the bright luminance was approximately 582 cd/m<sup>2</sup> at 19 V. They used a novel materials BDCM (*N,N*-bis{4-[2-(4-dicyanomethylene-6-methyl-4H-pyran-2-yl)ethylenyl]phenyl}aniline) as an emitter of red light [39]. Kido et al. successfully obtained blue-colour, green-colour and white-colour OLEDs, corresponding to a very high PE performance of 36 lm/W, 52 lm/W and 34 lm/W, respectively. They fabricated green phosphorescent OLEDs with a device configuration of indium tin oxide (ITO)/poly(3,4-ethylenedioxythiophene): poly(styrenesulfonate) (PEDOT:PSS)/poly(9,9-dioctyl-fluorene-alt-*N*-(4-butylphenyl)-diphenylamine)(TFB)/host:12 wt% Ir(ppy)<sub>3</sub>/1,3,5-tris(*N*-phenylbenzimidazol-2-yl)benzene (TPBi)/lithium 8-quinolate (Liq)/Al. In these OLED, TPBi was an ETL. In the

blue OLEDs, Kido et al. used 4,4'-(3,3'-bi(9H-carbazole)-9,9'-diyl)bis(2,6-diphenyl)benzene (13, BCzTPh) and 4,4'-(3,3'-bi(9H-carbazole)-9,9'-diyl)bis(*N,N*-diphenyl)aniline (16, BCzTPA) as host molecules and 2-propanol soluble 1,3-bis(3-(diphenylphosphoryl)phenyl)benzene (BPOPb) as an ETL. The device architecture was ITO/PEDOT:PSS/TFB/host:12 wt% FIrpic/BPOPb/Liq/Al [40]. Luszczynska et al. described the electroluminescence of five bithiophene disubstituted 1,3,4-thiadiazole bithiophene as materials for use in organic optoelectronics. The best luminance, 750 cd/m<sup>2</sup>, was achieved for 2,5-bis(5-octyl-2,2'-bithiophene-5-yl)-1,3,4-thiadiazole, with luminous efficiency exceeding 0.4 cd/A [41]. A device showing bluish-green light with a maximum brightness of 8264 cd/m<sup>2</sup> and a maximum current efficiency of 3.96 cd/A was fabricated by Ben Zhong Tang et al. They manufactured multilayer non-doped OLED with a configuration of ITO/HATCN/NPB/X 10% 20 nm/TPBi/LiF/Al. In these structures, the dipyrazine[2,3-*f*:2',3'-*h*]quinoxaline-2,3,6,7,10,11-hexacarbonitrile (HATCN) serves as a hole injection layer and *N,N*-bis(1-naphthyl)-*N,N*-diphenylbenzidine (NPB) and 1,3,5-tris(*N*-phenylbenzimidazol-2-yl)benzene (TPBi) work as hole-transporting and electron-transporting layers, respectively [42]. Due to the fact that the work concerns pyrazolo[3,4-*b*]quinolines, we should mention their earlier use in electroluminescent cells. Tao et al. [43] constructed a multi-layered cell based on 1-methyl-3-phenyl-6-*N,N*-dimethyl-1*H*-pyrazolo[3,4-*b*]quinoline. The device emitted a green light with a maximum luminance of 37,000 cd/m<sup>2</sup> and luminescent efficiency of 6.0 cd/A [43]. The same group applied thermally stable spirobifluorene-based 1*H*-pyrazolo[3,4-*b*]quinoline (spiro-PQ) as a luminophore in an OLED device with a configuration of ITO/NPB/CBP/TPBi + spiro-PQ/TPBi/Ag. The bright blue luminance exceeded 20,000 cd/m<sup>2</sup> with CIE coordinates (0.14; 0.17) [44]. Yanhu Li et al. [45] presented devices based on these oligofluorenes which exhibited highly efficient deep-blue electroluminescence. The double-layered device with PPO-TF3 as emitter shows a maximum current efficiency of 1.88 cd/A and a maximum external quantum efficiency of 3.39% with Commission Internationale de l'Eclairage (CIE) coordinates of (0.16, 0.09), which are very close to the National Television Standards Committee's blue standard [45]. A double-layer device ITO/DNCz/Alq3/LiF/Al was presented by Ki-Soo Kim et al. [46]. The devices showed a yellowish-green emission originating from Alq3 and used DNCz (9-ethyl-3-(naphthalene-2-yl)-6-(naphthalene-3-yl)-9*H*-carbazole) as a hole-transporting material. The luminance of this EL diode was approximately 18,600 cd/m<sup>2</sup>. Additionally, Ki-Soo Kim et al. described a multilayer device with a ITO/DNTPD/NPD/TCzPB (1,3,5-tris[4-(*N*-carbazolyl)phenyl]benzene) + Ir(ppy)<sub>3</sub>/BCP/Alq3/LiF/Al structure with a luminance of 27,200 cd/m<sup>2</sup> (17.6 cd/A at 18.0 V). TCzPB is a promising host material for phosphorescent dopants [46].

To date, many low-molecular compounds have been developed, and their usefulness for organic electronics has been positively confirmed. However, despite this, many research groups still conduct research on the preparation of new compounds and check their usefulness for organic optoelectronics. The activity of our group is in line with this research trend.

The main goal of this paper is a description of the photophysical properties of newly synthesized trifluoromethyl substituted low-molecular 1*H*-pyrazolo[3,4-*b*]quinolines Mol<sub>x</sub> (*x* = 1, 2, 3, 4). The mentioned compounds exhibit high light absorbance and electroluminescent properties. We describe their optical characteristics and verify their potential application in the fabrication of organic light emitting diodes (OLEDs) and organic photovoltaic devices (OPV).

The organization of the work is as follows. Section 2 outlines the procedure for the preparation of 1*H*-pyrazolo[3,4-*b*]quinoline dyes Mol<sub>x</sub> (*x* = 1, 2, 3, 4) compounds and their chemical characterization. Section 3 is devoted to a presentation of the equipment and methods used in the characterization of the materials and fabricated optoelectronic structures. In Section 4, the architectures of the fabricated solar cells and OLED structures are presented. In Section 5, we present the experimental results and their discussion.

## 2. Materials

### 2.1. Synthesis

The following organic materials 1*H*-pyrazolo[3,4-*b*]quinolines derivatives (Molx), namely 1-methyl-3-phenyl-6-CF<sub>3</sub>-1*H*-pyrazolo[3,4-*b*]quinoline (Mol1), 1-phenyl-3-methyl-6-CF<sub>3</sub>-1*H*-pyrazolo[3,4-*b*]quinoline (Mol2), 1,3-diphenyl-6-CF<sub>3</sub>-1*H*-pyrazolo[3,4-*b*]quinoline (Mol3) and 1,3-dimethyl-6-CF<sub>3</sub>-1*H*-pyrazolo[3,4-*b*]quinoline (Mol4), were tested for their use in optoelectronic devices. Their chemical structures are presented in Figure 1.

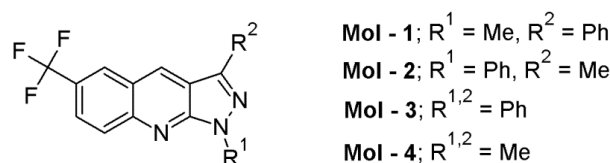


**Figure 1.** Chemical structures of investigated CF<sub>3</sub>-substituted 1*H*-pyrazolo[3,4-*b*]quinolines.

The trifluoromethyl substituted 1*H*-pyrazolo[3,4-*b*]quinolines (3) were synthesized according to procedure depicted in Figure 2.

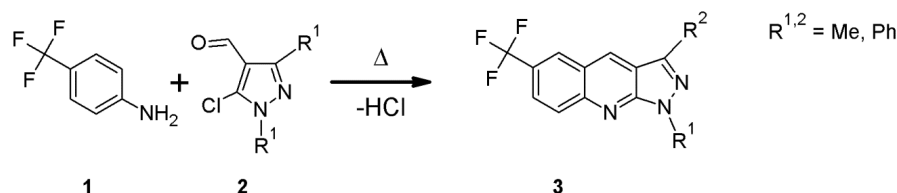


**Figure 2.** Synthetic procedure for CF<sub>3</sub>-substituted 1*H*-pyrazolo[3,4-*b*]quinolines.

Thus, *p*-trifluoromethylaniline (1) was heated with 5-chloro-4-formyl-1,3-disubstituted pyrazoles (2) without solvent. The pyrazole derivatives (2) were prepared by Vilsmeier–Haack formylation of appropriate pyrazolones. The details of these procedures are described in the paper published by Brack and Villsmeier/Haack, respectively [47,48].

### Synthetic Procedures

<sup>1</sup>H and <sup>13</sup>C NMR spectra were carried out by means of a Bruker Avance III 300 spectrometer (Billerica, MA, USA) operating at 300 and 75 MHz, respectively. Samples were dissolved in CDCl<sub>3</sub>, with TMS as an internal standard. The melting points were determined on a Stuart SMP3 melting point apparatus (capillary), and they were uncorrected. Elemental analyses were conducted at Elementar Vario MICRO cube.

6-(Trifluoromethyl)-1-methyl-3-phenyl-1*H*-pyrazolo[3,4-*b*]quinoline (Mol1): 4-(trifluoromethyl)aniline (805 mg, 5 mmol) was mixed with 5-chloro-1-methyl-3-phenyl-1*H*-pyrazole-4-carbaldehyde (993 mg, 5 mmol) and heated on a sand bath until the temperature reached 190 °C; it was then maintained in that temperature for 60 min. The mixture was then allowed to cool to room temperature, and the resulting brown-yellow solid was dissolved in chloroform and flushed through Aluminium Oxide 60. The resulting yellow solid was crystallized twice from toluene to yield 1.13 g (77%) of yellow fluorescent needles, m.p. 161–161.5 °C. <sup>1</sup>H NMR (CDCl<sub>3</sub>, δ, ppm): 8.95 (s, 1H, Ar-H), 8.32 (broad s, 1H, Ar-H), 8.21 (dd, *J* = 9.1, 0.6 Hz, 1H, Ar-H), 8.06–8.02 (m, 2H, Ar-H), 7.90 (dd, *J* = 9.1, 2.0 Hz, 1H, Ar-H), 7.60–7.55 (m, 2H, Ar-H), 7.51–7.45 (m, 1H, Ar-H), 4.30 (s, 3H, CH<sub>3</sub>); <sup>13</sup>C NMR (CDCl<sub>3</sub>, δ, ppm): 152.0, 148.8, 143.2, 132.5, 132.2, 129.5, 129.1, 128.9, 127.3 (q, *J*<sub>C-F</sub> = 4.7 Hz), 127.1, 126.0 (q, *J*<sub>C-F</sub> = 2.3 Hz), 125.5 (q, *J*<sub>C-F</sub> = 32.0 Hz), 122.8, 115.7, 34.1; Found: C, 66.01; H, 3.75; N, 12.90; C<sub>18</sub>H<sub>12</sub>F<sub>3</sub>N<sub>3</sub> requires: C, 66.05; H, 3.70; N 12.84.

6-(Trifluoromethyl)-3-methyl-1-phenyl-1*H*-pyrazolo[3,4-*b*]quinoline (Mol2): 4-(trifluoromethyl)aniline (970 mg, 6 mmol) was mixed with 5-chloro-3-methyl-1-phenyl-1*H*-pyrazole-4-carbaldehyde (1190 mg, 6 mmol) and a few drops of sulfolane and heated on a sand bath until the temperature reached 220 °C; it was then maintained at that temperature for 45 min. The mixture was then allowed to cool to room temperature, and the resulting

brown-yellow solid was treated with methanol in an ultrasonic bath for a few minutes. A yellow solid was filtered off, dissolved in chloroform and flashed through Aluminium Oxide 60. The resulting solid was chromatographed on a SilicaGel 60 column with toluene to yield 600 mg (31%) of yellow plates, m.p. 143.5–144 °C. <sup>1</sup>H NMR (CDCl<sub>3</sub>, δ, ppm): 8.62 (s, 1H, Ar-H), 8.48–8.44 (m, 2H, Ar-H), 8.29 (broad s, 1H, Ar-H), 8.24 (dd, *J* = 9.1, 0.6 Hz, 1H, Ar-H), 7.90 (dd, *J* = 9.1, 2.0 Hz, 1H, Ar-H), 7.59–7.52 (m, 2H, Ar-H), 7.33–7.28 (m, 1H, Ar-H), 2.77 (s, 3H, CH<sub>3</sub>); <sup>13</sup>C NMR (CDCl<sub>3</sub>, δ, ppm): 151.1, 149.0, 143.6, 139.6, 130.8, 130.1, 129.1, 127.2 (q, *J*<sub>C-F</sub> = 4.5 Hz), 125.9 (q, *J*<sub>C-F</sub> = 3.0 Hz), 125.9 (q, *J*<sub>C-F</sub> = 32.6 Hz), 125.3, 122.6, 120.3, 119.1, 12.8; Found: C, 66.10; H, 3.80; N, 12.77; C<sub>18</sub>H<sub>12</sub>F<sub>3</sub>N<sub>3</sub> requires: C, 66.05; H, 3.70; N 12.84.

6-(Trifluoromethyl)-1,3-diphenyl-1*H*-pyrazolo[3,4-*b*]quinoline (Mol3): 4-(trifluoromethyl) aniline (1.61 g, 10 mmol) was mixed with 5-chloro-1,3-diphenyl-1*H*-pyrazole-4-carbaldehyde (2.83 g, 10 mmol) and heated on a sand bath until the temperature reached 180 °C; it was then maintained in that temperature for 60 min. Then the mixture was allowed to cool to room temperature, and the resulting brown solid was dissolved in chloroform and flashed through Aluminium Oxide 60. The resulting yellow solid was crystallized from DMF to yield 2.20 g (57%) of deep-yellow crystalline powder, m.p. 175 °C. <sup>1</sup>H NMR (CDCl<sub>3</sub>, δ, ppm): 8.97 (s, 1H, Ar-H), 8.57–8.54 (m, 2H, Ar-H), 8.33 (broad s, 1H, Ar-H), 8.26 (dd, *J* = 9.0, 0.5 Hz, 1H, Ar-H), 8.13–8.10 (m, 2H, Ar-H), 7.91 (dd, *J* = 9.1, 2.0 Hz, 1H, Ar-H), 7.62–7.49 (m, 5H, Ar-H), 7.37–7.31 (m, 1H, Ar-H); <sup>13</sup>C NMR (CDCl<sub>3</sub>, δ, ppm): 151.5, 148.8, 144.7, 139.6, 132.2, 132.1, 130.1, 129.3, 129.2, 129.1, 127.5, 127.4 (q, *J*<sub>C-F</sub> = 4.7 Hz), 126.3 (q, *J*<sub>C-F</sub> = 32.3 Hz), 126.1 (q, *J*<sub>C-F</sub> = 2.6 Hz), 125.8, 124.1 (q, *J*<sub>C-F</sub> = 270 Hz), 123.2, 120.8, 117.3; Found: C, 70.93; H, 3.57; N, 10.85; C<sub>23</sub>H<sub>14</sub>F<sub>3</sub>N<sub>3</sub> requires: C, 70.95; H, 3.62; N 10.79.

6-(Trifluoromethyl)-1,3-dimethyl-1*H*-pyrazolo[3,4-*b*]quinoline (Mol4): 4-(trifluoromethyl) aniline (970 mg, 6 mmol) was mixed with 5-chloro-1,3-dimethyl-1*H*-pyrazole-4-carbaldehyde (950 mg, 6 mmol) and a few drops of sulfolane and heated on a sand bath until the temperature reached 200 °C; it was then maintained in that temperature for 45 min. The mixture was then allowed to cool to room temperature, and the resulting brown-yellow solid was treated with methanol in an ultrasonic bath for a few minutes. The resulting yellow solid was filtered off, dissolved in chloroform and flashed through Aluminium Oxide 60. The solid was chromatographed in a SilicaGel 60 column with toluene to yield 450 mg (28%) of yellowish crystalline powder, m.p. 140–141 °C. <sup>1</sup>H NMR (CDCl<sub>3</sub>, δ, ppm): 8.60 (s, 1H, Ar-H), 8.28 (broad s, 1H, Ar-H), 8.18 (broad d, *J* = 9.1 Hz, 1H, Ar-H), 7.87 (dd, *J* = 9.1, 2.1 Hz, 1H, Ar-H), 4.18 (s, 3H, N-CH<sub>3</sub>), 2.71 (s, 3H, Ar-CH<sub>3</sub>); <sup>13</sup>C NMR (CDCl<sub>3</sub>, δ, ppm): 152.5, 149.7, 142.2, 131.6, 130.0, 128.1 (q, *J*<sub>C-F</sub> = 4.7 Hz), 126.4 (q, *J*<sub>C-F</sub> = 2.6 Hz), 122.8, 118.1, 34.3, 13.4; Found: C, 58.78; H, 3.82; N, 15.92; C<sub>13</sub>H<sub>10</sub>F<sub>3</sub>N<sub>3</sub> requires: C, 58.87; H, 3.80; N 15.84.

### 3. Equipment and Methods

As part of the studies presented here, theoretical analyses and experimental research were carried out. The theoretical analyses involved molecular conformations and determination of HOMO-LUMO levels of the Mol<sub>x</sub> compound. Optical analysis of the photovoltaic structures was carried out. Calculations of the light intensity distribution and the density of the generated excitons in the photovoltaic cells were performed using the 2 × 2 matrix method presented in our earlier works [49–51]. In experimental studies, the absorption properties of the developed compounds were determined, and the complex refractive index of the bulk heterostructure composed of the polymer-PVK blend was determined. The apparatus and measurement methods used are presented below. The produced structures of the photovoltaic cells and OLEDs were tested using the measurement systems presented in our previous papers [52,53]. Optical analysis of the photovoltaic structures was carried out. The light intensity distribution and the density of the generated excitons in the photovoltaic cells were calculated using the 2 × 2 matrix method presented in our previous works [49–51].

### 3.1. DFT Calculation

Quantum chemical calculations were performed using the PL-Grid Infrastructure and resources provided by the ACC Cyfronet AGH (Kraków, Poland). DFT and TDFT calculations were carried out with the Gaussian 16 package (Revision B.01, Wallingford, CT, USA) [54], based on the computational approach that has been successfully applied for the pyrazolo[3,4-*b*]quinolines and their derivatives [55–57]. The geometry optimization was performed using density-functional theory (DFT) and the B3LYP functional [58–60], together with a Dunning correlation-consistent, polarized valence [61], double- $\zeta$  basis set, cc-pVDZ. The photophysical properties were calculated as vertical electronic excitations from the minima of the ground-state, using the linear-response approach, the B3LYP/cc-pVDZ level of theory and the first six excited states. The solvent effect was taken into account by including the polarizable continuum model (PCM) [62] and acetonitrile as solvent. All obtained minima were confirmed by the absence of a negative frequency in the vibrational analysis. The simulated spectra were obtained as the sums of Gaussian functions centred at vertical excitation energies and scaled using the calculated oscillator strengths with a half-width at half-height parameter implemented in the GaussView 6.0.16 program.

### 3.2. Spectral and Time Resolved Measurements

Absorption spectra were recorded using a Shimadzu UV-2101 PC spectrometer (Markham, ON, Canada). Room-temperature and low-temperature (at 77 K) fluorescence spectra (with the correction for spectral sensitivity) were measured by a Hitachi F7000 fluorometer (Tokio, Japan). Phosphorescence was measured in a dibutyl ether matrix (at 77 K) using a Hitachi F7000 fluorometer (Tokio, Japan) with a chopping frequency 40 Hz. For time-resolved fluorescence measurements (time-correlated single-photon counting technique), a picosecond diode laser ( $\lambda = 400$  nm, 70 ps pulse duration) (IBH-UK) was used as the excitation source. The  $\chi^2$  test and the distribution of residuals were the main criteria in the evaluation of the quality of fit of the experimental decay curves. For steady-state fluorescence measurements, a 370 line was used. The fluorescence quantum yield measurements were carried out with quinine sulphate in 0.05 M H<sub>2</sub>SO<sub>4</sub> ( $\Phi_{\text{fl}} = 0.51$ ) [63] as an actinometer. The fluorescence studies were performed on deaerated samples. The acetonitrile and dibutyl ether used for the spectrophotometric measurements were purchased from AlfaAesar (HPLC grade, Gdańsk, Poland). Both absorption and steady state emission measurements were done with the aid of instruments collected at University of Agriculture, Kraków, Poland. Time-resolved fluorescence studies were measured at Jagiellonian University, Kraków, Poland.

### 3.3. Electrochemical Measurements

Cyclic voltammetry measurements were performed on a potentiostat (PalmSens3). A platinum wire ( $\varnothing = 0.5$  mm) and a platinum coil ( $\varnothing = 1.6$  mm) were used as a counter and working electrodes, respectively. A non-aqueous electrode (Ag/Ag<sup>+</sup>), designed and provided by ALS, was used as a quasi-reference electrode. The potential of the quasi-reference electrode was calibrated using ferrocene as an internal standard. A 0.1 M solution of Bu<sub>4</sub>NPF<sub>6</sub> (Aldrich  $\geq 99.0\%$ ) in acetonitrile (AlfaAesar HPLC grade was additionally dried with a molecular sieves 4 Å and distilled prior to use) was used as the electrolyte. The obtained potentials were additionally confirmed by independent differential pulse voltammetry measurements (DPV). Prior to the measurements, the solutions were purged with argon to remove residual oxygen.

### 3.4. Ellipsometry

The optical functions and thicknesses of the constituent layers of the solar cells produced were determined using the spectroscopic ellipsometry method. In this measurement technique, the ratio,  $\rho$ , of the Fresnel reflection coefficients for *s*- and *p*-polarized components is described by the following equation [52,64,65]:

$$\rho = \frac{r_p}{r_s} = \tan \psi e^{i\Delta} \quad (1)$$

where  $\psi$  and  $\Delta$  are the ellipsometric angles, named amplitude ratio and phase shift, respectively. The spectral characteristics of the ellipsometric angles  $\psi$  and  $\Delta$  were recorded using an ellipsometer. The theoretical characteristics of the ellipsometric angles, calculated from the assumed model of the examined structure, were then fitted to the experimental ones. The structure parameters assumed for the calculations, for which the best matching of theoretical and measurement characteristics were obtained, were taken as those which characterized the investigated structure. In our studies, we used a spectroscopic ellipsometer Woollam M2000 (J.A. Woollam Co., Inc., Lincoln, NE, USA) and CompleteEASE Software.

Examples of the spectral characteristics of the ellipsometric angles, appropriately measured and calculated for the active layer of the sample (glass/ITO/PEDOT:PSS/active layer), are shown in Figure 8. Measurements were made for angles  $\theta$  sample lighting  $60^\circ$ ,  $65^\circ$  and  $70^\circ$ , respectively. In all calculations for the active layers, we used the Tauc–Lorentz model with Gaussian oscillators, described as follows:

$$\varepsilon_{2\_NG} = A_{NG}e^{-\left(\frac{E-E_{0\_N}}{Bf_N}\right)^2} - A_{NG}e^{-\left(\frac{E+E_{0\_N}}{Bf_N}\right)^2} \quad (2)$$

where  $f_N = \frac{1}{2\sqrt{\ln 2}}$  and the fitting parameters are  $A_{NG}$ —amplitude,  $B$ —boarding,  $E_{0\_N}$ —oscillator energy,  $N$ —oscillators ( $N = 6$ , fitting for four Gaussian oscillators) [54,55,63,64,66].

#### 4. Solar Cells and OLEDs Fabrications

In our work, we present fabricated bulk heterojunction (BHJ) photovoltaic cells based on organic materials. The structure of the investigated sample was as follows: glass/ITO/PEDOT:PSS/organic active layer/aluminum (Al) (see Figure 3). The organic active layer was a blend of Molx + PDT, (where PDT is poly(3-decyloctifen2,5-diyl) and  $x = \text{Mol1, Mol2, Mol3, Mol4}$ —see Figure 1) dissolved in tetrahydrofurane THF (anhydrous, 99.9% Sigma-Aldrich). The ITO (indium oxide solid solution (II) oxide and tin (IV)), coated on glass, was the substrate in the structure of the BHJ photovoltaic cells. The sheet resistance of ITO was approximately  $15 \Omega/\text{sq}$ . The ITO underwent a cleaning in an ultrasonic cleaner using isopropanol, acetone, detergent and distilled water. A thin layer of PEDOT:PSS [poly(3,4-ethylenedioxythiophene): polystyrenesulfonic acid]—was then applied to the prepared substrate by the spin coating method. The thin layer PEDOT:PSS (1.3 wt% dispersion in  $\text{H}_2\text{O}$ , conductive grade) was heated in a vacuum at  $100^\circ\text{C}$  for 30 min. The organic active layer Molx + PDT was sandwiched between PEDOT:PSS and an aluminium electrode. Finally, an aluminium (Al) anode (100 nm) was deposited by evaporation in a high vacuum ( $10^{-6}$  bar). The resulting photovoltaic (BHJ) cells had an area of  $15 \times 15 \text{ mm}^2$ . PDT, THF, acetone, isopropanol and ITO was purchased from Sigma-Aldrich. The effect of the organic active layer on the performance of PDT + Molx cells were investigated using a current source Keithley 2400 SourceMeter in the dark and under illumination with a tungsten lamp with a fixed power density of  $1.3 \text{ mW}/\text{cm}^2$ .

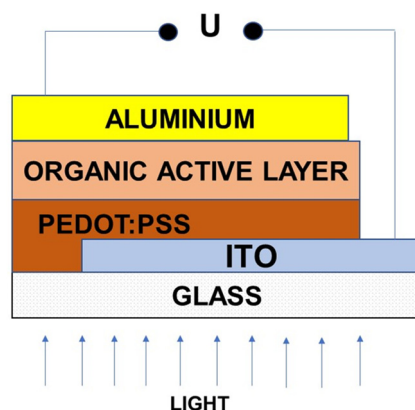
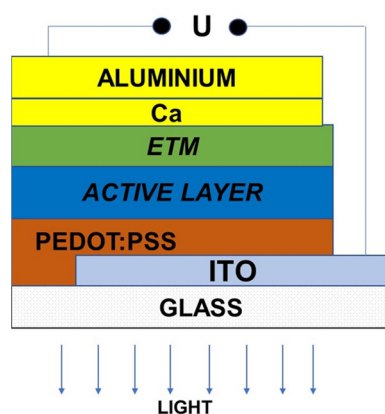


Figure 3. Bulk heterojunction architecture of investigated devices.

The structure of the prepared organic light-emitting diodes (OLEDs) is shown in Figure 4. These structures had the following configuration—glass/ITO/PEDOT:PSS/active layer/ETM/Ca/Al. On the glass/ITO sample was a spin-coated PEDOT:PSS layer. The thin PEDOT:PSS layer was dried at 100 °C for 45 min to remove the remains of water. In the next step, the emission layer, PVK + Molx (where  $x$  was 1, 2, 3, 4), was applied using a spin-coater on a glass/ITO substrate. The active layer (Molx + PVK) was a mixture of luminophores (Mol1, Mol2, Mol3, Mol4) and PVK were dissolved in tetrahydrofuran (THF). Then, on top of this sample, a 2-[3,5-bis(4-phenyl-2-quinolyl)phenyl]-4-phenylquinoline (Tris-Q)) layer, as an electron transparent material (ETM) was spin-coated. The Ca/Al electrode was evaporated in a high vacuum ( $10^{-6}$  bar) on the organic active layer. In the studied structures, the ITO is a positive electrode and the Ca/Al is a negative electrode.



**Figure 4.** The OLED's structure ITO/PEDOT:PSS/active layer/ETM/Ca/Al.

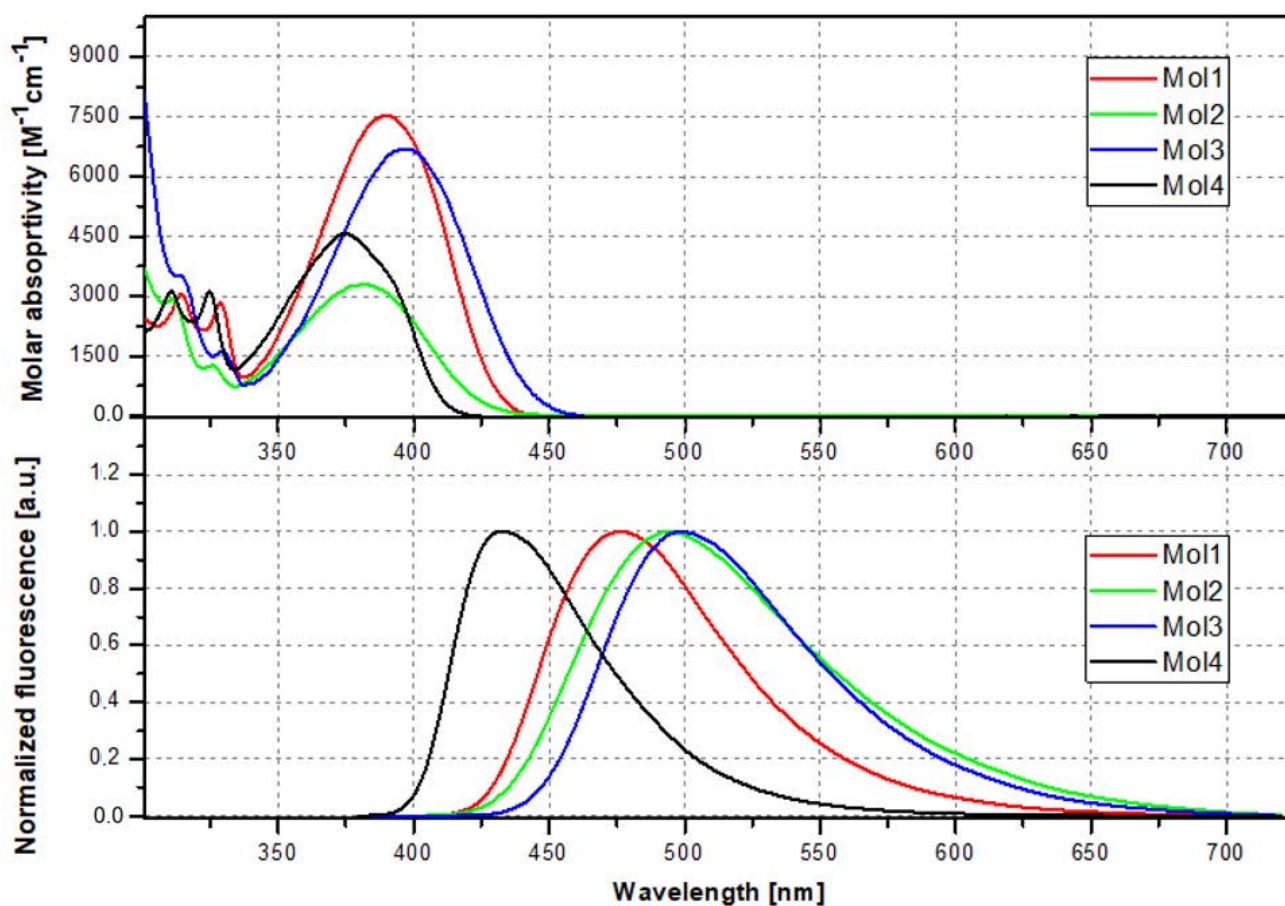
## 5. Results and Discussion

### 5.1. Photophysical Properties

Room-temperature absorption and fluorescence spectra of the investigated compounds are presented in Figure 5.

Absorption and emission data are shown in Table 1. Similarly to 1,3-dimethylpyrazolo[3,4-*b*]quinoline [67], Mol4 exhibits a vibronic structure of the lowest absorption band, with a maximum located at 375 nm. This slight vibrational structure (occurring even in polar acetonitrile), along with a moderate extinction coefficient ( $\epsilon = 4600 \text{ M}^{-1} \text{ cm}^{-1}$ ), may indicate the presence of  $\pi, \pi^* \leftarrow S_0$  transition. The low energy band of the phenyl-decorated compounds shows clear red shift compared to the 1,3-dimethyl counterpart (Mol4). The shift depends on both the number of phenyl substituents attached to the pyrazole part and their location. Hence, the most pronounced bathochromic shift was observed for Mol3 (with two phenyl groups). Moreover, the phenyl attached to the 3rd position of the pyrazole part induces a larger bathochromic shift of absorption maximum than in the 1st position. Although the absorption maxima significantly differ from one another (381 nm and 390 for Mol2 and Mol1, respectively), the HOMO/LUMO energy gaps are practically the same (Figure 5). This is in line with quantum chemical calculations predicting the absorption maximum at 411 nm ( $\epsilon = 7850 \text{ M}^{-1} \text{ cm}^{-1}$ ) for Mol1 and at 413 nm ( $\epsilon = 2450 \text{ M}^{-1} \text{ cm}^{-1}$ ) for Mol2. Therefore, the difference in absorption maxima can be justified in terms of the presence of two rotamers in solution: with phenyl in or out of the pyrazoloquinoline plane. To verify this hypothesis, 2D relaxed potential energy surfaces were built by varying the dihedral angle between the phenyl attached to the 1st or 3rd position of the pyrazole and the pyrazoloquinoline core (Figure S2). Based on those results and available thermal energy at 295 K ( $3RT = 0.077 \text{ eV}$ ), two conformations were chosen for each mono-phenyl functionalized molecule under study (see Figure S3). Next, the lowest energy excitation, along with molar absorptivity, were predicted, and the results are listed in Table S1. The photophysical behaviour of Mol2 with the phenyl

twisted out of plane (Mol2t,  $\lambda_{abs,cal} = 388 \text{ nm}$ ,  $\epsilon_{cal} = 3450 \text{ M}^{-1} \text{ cm}^{-1}$ ) resembles the optical properties of the parent molecule (Mol4,  $\lambda_{abs,cal} = 388 \text{ nm}$ ,  $\epsilon_{cal} = 4100 \text{ M}^{-1} \text{ cm}^{-1}$ ). Although a full perpendicular twist of 1-phenyl substituent is rather unlikely due to a large energy barrier (Mol2 0.149 eV), the presence of a sixty degree twist is highly probable. Such a wide range of torsional angles makes feasible the existence of two opposite conformations (planar Mol2p and twisted rotamer Mol2t). Bearing in mind that the predicted molar absorptivity of Mol2p is significantly lower than that for Mol2t, it is evident that the superposition of these two bands may lead to the formation of a new band with an absorption maximum located close to that of Mol4. The simulated averaged absorption spectra, presented in Figure S4 in the Supplementary Materials, well reproduce the experimental one in terms of the relative energetic positions and intensity of the absorption bands. The same reasoning may be applied in the context of Mol1 (energy barrier 0.153 eV). In this case, a red-shifted absorption is related to the high absorptivity of global energy conformation (Mol1p, 3-phenyl twisted by  $24^\circ$  with respect to the pyrazoloquinoline plane,  $\lambda_{abs,cal} = 411 \text{ nm}$ ,  $\epsilon_{cal} = 7850 \text{ M}^{-1} \text{ cm}^{-1}$ ), which makes the UV band of a more distorted rotamer Mol1t less visible ( $\lambda_{abs,cal} = 387 \text{ nm}$ ,  $\epsilon_{cal} = 6000 \text{ M}^{-1} \text{ cm}^{-1}$ , see Figure S4). Finally, the observed absorption maximum of Mol3 results from the additive effect of two phenyl substituents attached to the pyrazoloquinoline core.

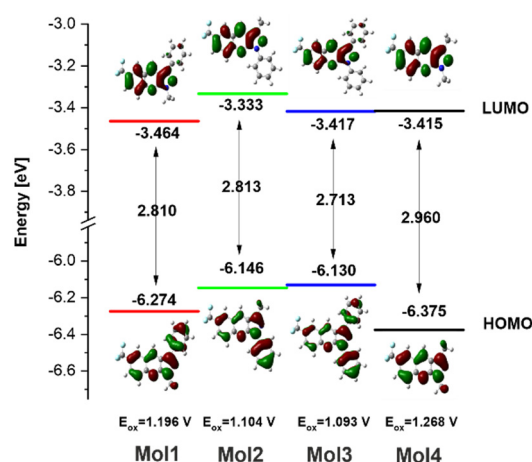


**Figure 5.** UV-Vis absorption (**top**) and emission (**bottom**) spectra of the compounds under study in acetonitrile: Mol1 (**red**); Mol2 (**green**); Mol3 (**blue**); Mol4 (**black**).

**Table 1.** Absorption and Emission Parameters of the Investigated Dyes Dissolved in Acetonitrile.

Compound	Solvent	$\lambda_{abs}$ (nm)	$\epsilon$ ( $M^{-1} cm^{-1}$ )	$\lambda_{fl}$ (nm)	$\Phi_{fl}$	$\tau_{fl}$ (ns)	$k_{nr}$ ( $\times 10^7 s^{-1}$ )	$k_r$ ( $\times 10^7 s^{-1}$ )
Mol1	ACN	390	7500	476	0.41	31.62	1.87	1.30
Mol2	ACN	381	3300	495	0.14	20.57	4.18	0.68
Mol3	ACN	397	6700	500	0.27	28.97	2.52	0.93
Mol4	ACN	375	4600	433	0.73	34.66	0.78	2.11

The Gaussian shape of the absorption band, along with the observed red shift, may point to the partial charge transfer character of the first singlet excited state in Mol2 and Mol3 [68]. It seems that the phenyl at the 1st position plays a crucial role in the formation of charge transfer state due to a strong electronic conjugation between this substituent and the  $CF_3$  group (see HOMO/LUMO contours of orbitals for Mol2). Moreover, the attachment of phenyl to the nitrogen atom of pyrazole (stronger electronegativity than the carbon atom), along with the close vicinity of a positively charged centre (located at the carbon atom connecting the nitrogen of the quinoline and that of pyrazole) (Figure S6) may favour charge migration in this compound. As a consequence, a full electron density shift from phenyl at the 1st position to the pyrazoloquinoline skeleton occurs upon excitation to the first singlet excited state, while in Mol1 residual charge density is still noticeable at the 3-phenyl substituent (see LUMO contours of orbitals, Figure 6). This behaviour is also reflected in emission properties. Mol2 exhibits the weakest fluorescence and the shortest fluorescence lifetime from all the studied compounds, which may indeed indicate the existence of the photoinduced electron transfer process being responsible for fluorescence quenching. It is very likely that this process is partially suppressed in Mol3 due to the presence of additional phenyl at the 3rd position. Finally, some distortions of Mol1 from planarity may result in a smaller electronic conjugation and then weaker fluorescence quenching caused by the photoinduced electron transfer process, as compared to Mol2. The lack of an electron-rich phenyl substituent and the small Stokes shift of Mol4 point to the fact that the first singlet excited state is most probably of the  $\pi, \pi^*$  character. Summing up, the energy of the singlet excited state is modulated both by the number of phenyl substituents and their location. In addition, the character of the singlet excited state changes from  $^1(\pi, \pi^*)$  to  $^1CT$  with the presence of the phenyl group.

**Figure 6.** Oxidation potentials HOMO–LUMO energy levels and energy band gaps of the investigated dyes.

Depending on the mechanism of the singlet energy deactivation, electroluminescent materials can be divided into three categories: fluorescent emitters, phosphorescent emitters and thermally activated delayed fluorescence (TADF) emitters. In order to classify the investigated dyes to one of the above-mentioned groups, low-temperature phosphorescence measurements were performed.

As depicted in Figure S7 in the Supplementary data, the studied dyes exhibit only low-temperature fluorescence. With the course of the experiment, no signal of phosphorescence was detected, confirming that the emission occurs only from the first singlet excited state. Hence, a competitive deactivation pathway via an intersystem crossing process can be ruled out. Taking into account the above-mentioned considerations, one can classify the studied dyes as the first generation of OLED materials (fluorescent materials).

### 5.2. Electrochemistry

In order to prepare the electroluminescent cell, it is required to know the HOMO/LUMO energy levels of the emissive material tested for OLEDs. The knowledge of these parameters enables one to choose and apply such hole/electron transporting materials, which will be efficient in the recombination of the injected hole/electron pair. One of the methods commonly used for determination of HOMO/LUMO energy levels is cyclic voltammetry. It is a simple and useful technique to compare the relative energy levels for the series of derivatives in the same class. HOMO energy levels were calculated using this well-known equation:  $E_{HOMO} = -(1.4 \pm 0.1) \cdot qE_{ox} - (4.6 \pm 0.08) \text{ eV}$  [69]. ( $E_{ox}$ —The onset oxidation potential taken from the cyclic voltammogram;  $q$ —Electric charge). The LUMO levels have been deduced from the optical band gap values [70]. Optical band gap was evaluated from the absorption spectra using the Tauc method [70]. The obtained values of oxidation potentials, HOMO/LUMO energy levels and energy band gaps are presented in Figure 6.

All the investigated pyrazoloquinolines exhibit a weakly reversible oxidation peak at the platinum electrode with reference to the non-aqueous reference electrode Ag/Ag<sup>+</sup> (Figure 7). Both Mol4 ( $E_{ox} = 1.268 \text{ V}$ ) and Mol1 ( $E_{ox} = 1.196 \text{ V}$ ) display a clear single oxidation peak, while Mol3 exhibits dual oxidation peaks at 1.093 V and 1.198 V, appearing during an anodic scan. In the case of the Mol2 derivative, the oxidation profile may resemble a dual character (1.104 V, 1.239 V); however, the second peak is hardly visible and is irreversible. Therefore, it was not taken into consideration during further analysis. The analysis of the values of oxidation potentials confirmed that the CV profile of Mol3 is a superposition of two oxidation peaks: one related to the oxidation of 1-phenyl-*N*-pyrazol and the second associated with phenyl oxidation at the third position.

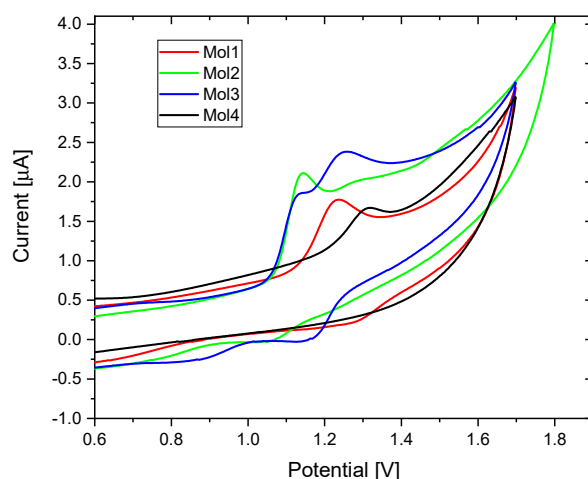


**Figure 7.** Cyclic voltammetry plots of compounds under the study referenced to the ferrocene/ferrocenium couple: Mol1, Mol2, Mol3 and Mol4.

In each phenyl derivative under study, the presence of phenyl leads to an increase of electron density on the core, which results in an easier oxidation process of the compound (higher HOMO energy). It is worth noting that the different locations of phenyl in the Mol1 and Mol2 compounds can modulate the HOMO energy level in various ways. Due to a strong interaction between 1-phenyl and CF<sub>3</sub>, the charge density of the PQ core is significantly enriched, resulting in the increase of HOMO energy level. This increase is

smaller in Mol1 due to less effective charge/electron injection to the core by 3-phenyl, twisted with respect to the PQ skeleton. Finally, the value of HOMO/LUMO of Mol3 is the net result of the Mol1 and Mol2 physicochemical properties.

### 5.3. Complex Refractive Index and Film Thickness

The complex refractive index of the active layer Mol3 + PDT over the PEDOT:PSS/ITO/glass substrate was determined using the spectroscopy ellipsometry method described in the previous section. In Figure 8, the spectral characteristics of the ellipsometric angles  $\Psi$  and  $\Delta$  for three different illumination angles of the structure ( $\theta = 60^\circ$ ,  $65^\circ$  and  $70^\circ$ ), registered for Mol3 + poly (3-decylthiophene-2,5-diyl), are presented. The registered (experimental) characteristics are plotted with individual continuous coloured lines, and theoretical approximations corresponding to the best fit are plotted with continuous black lines. For each illumination angle,  $\theta$ , a perfect agreement of the theoretical characteristics with the experimental characteristics is visible. The determined complex refractive index Mol3 + poly (3-decylthiophen-2,5-diyl) is presented in Figure 9. The dispersion characteristic of the refractive index,  $N(\lambda)$ , is drawn in black and the dispersion characteristic of the extinction coefficient,  $\kappa(\lambda)$ , is drawn in blue. The characteristic  $\kappa(\lambda)$  shows a wide absorption peak which, for the wavelength  $\lambda = 550$  nm, reaches the maximum value of  $\kappa_{max} = 0.6$ . The ellipsometric measurements also determined the thickness of the active layers in the photovoltaic structures made. The determined values are listed in the second column in Table 2.

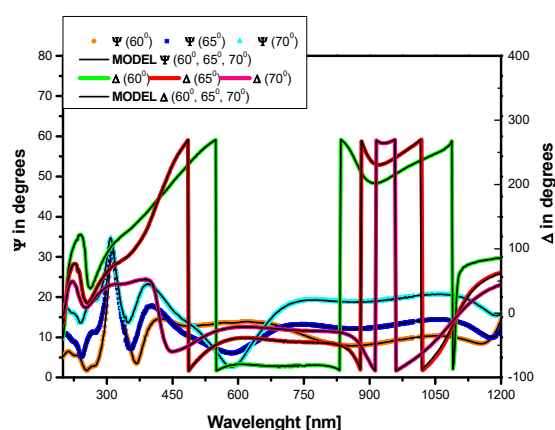


**Figure 8.** Spectral dependence of ellipsometric angles  $\Psi$  and  $\Delta$  for the Mol3 + poly(3-decylthiophen-2,5-diyl) layer over the PEDOT:PSS layer of the ITO film on the glass substrate.

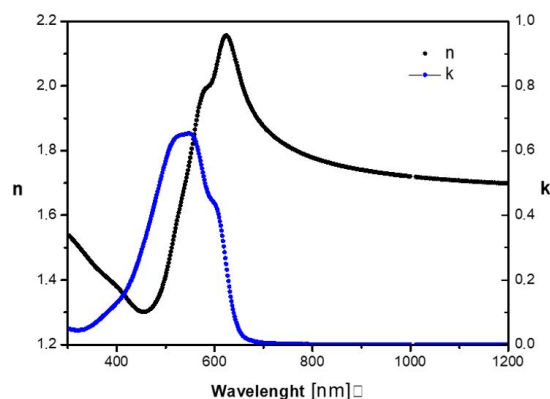


**Figure 9.** Dispersion relations of refractive index  $n$  and extinction coefficient  $k$  for the Mol3 + poly(3-decylthiophen-2,5-diyl) layer over the PEDOT:PSS layer of the ITO film on the glass substrate.

**Table 2.** Principal parameters obtained for the manufactured organic photovoltaic devices:  $V_{OC}$ —Open Circuit Voltage,  $J_{SC}$ —Current Density,  $FF$ —Fill Factor,  $\eta$ —Power Efficiency.

Photovoltaic Cell	Thickness Molx + PDT (nm)	$J_{SC}$ ( $\mu\text{A}/\text{cm}^2$ )	$V_{OC}$ (V)	$FF$	$\eta$ (%)
ITO/PEDOT:PSS/Mol1 + PDT/Al	102.9	30.88	0.70	0.20	0.32
ITO/PEDOT:PSS/Mol2 + PDT/Al	105.6	24.71	0.85	0.21	0.33
ITO/PEDOT:PSS/Mol3 + PDT/Al	111.0	32.81	0.78	0.19	0.38
ITO/PEDOT:PSS/Mol4 + PDT/Al	98.5	19.70	0.64	0.21	0.21

Figure 10a shows the light intensity distribution in the structure of the photovoltaic cell ITO/PEDOT:PSS/PDT + Mol3/Al. Figure 10b shows the density distribution of the generated excitons,  $G$ , in this photovoltaic cell. The complex refractive index presented in Figure 9 was taken for the calculations. The refractive indices of the materials of the remaining layers were taken from the literature [49,50].

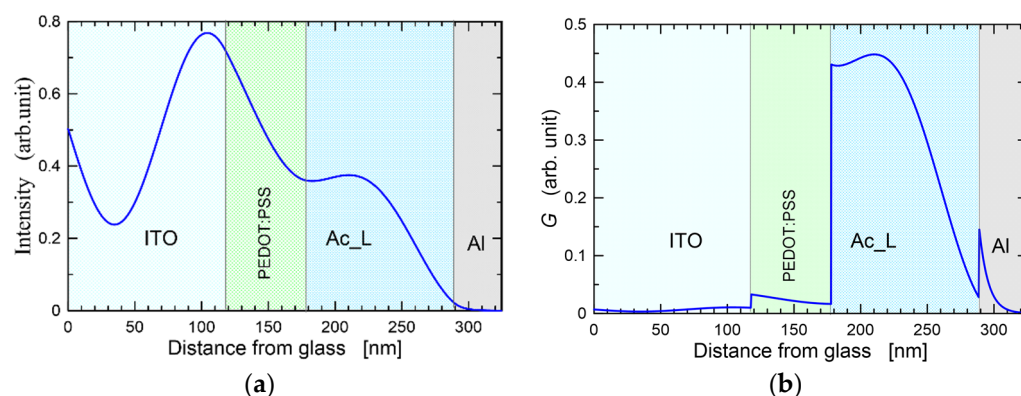


**Figure 10.** Distribution of light intensity (a) and distribution of generated excitons density (b) in solar cell ITO/PEDOT:PSS/PDT + Mol3/Al  $\lambda = 560$  nm.

Figure 10a shows the maximums and minimums of the interference, which are the result of the formation of an optical standing wave in the structure of a photovoltaic cell. The standing wave node is formed near the Ac\_L/Al surface, where the largest antinode in the ITO layer is formed. This situation is not optimal and has a negative impact on the efficiency of the solar cell. The optimal situation is when the maximal antinode is in the area of the active layer. However, this requires the use of a TCE layer, which will move the antinode away from the surface of the aluminium electrode. Figure 10b shows the density distribution of the generated excitons,  $G$ , as a function of the distance from the surface of the substrate glass. As can be seen, the highest densities of generated excitons occur in the area of the active layer.

#### 5.4. OPV Devices

Comparisons of the dark and under illumination current density–voltage ( $J$ – $V$ ) characteristics of ITO/PEDOT:PSS/PDT + Molx/Al are shown in Figure 11.

For whole fabricated photovoltaic cells, the fill factor,  $FF$ , current density,  $J_{SC}$ , in the short circuit obtained without any external applied voltage or potential and open-circuit voltage,  $V_{OC}$ , were determined from current–voltage characteristics. For device 3, with the configuration ITO/PEDOT:PSS/Mol3 + PDT/Al, the thickness of the active layer (Mol3 + PDT) was equal 111.0 nm. In this architecture, the mixture of 1-phenyl-3-phenyl-6-CF<sub>3</sub>-1*H*-pyrazolo[3,4-*b*]quinoline (Mol3) and poly(3-butylthiophene-2,5-diyl)—PDT—was used as the active layer, and the power conversion efficiency,  $\eta$ , was approximately 0.38% for a current density  $J_{SC} = 32.81 \mu\text{A}/\text{cm}^2$  and open-circuit voltage  $V_{OC} = 0.78$  V. Higher  $V_{OC}$  values equal to 0.85 V were achieved for cells based on a blend of Mol2 and PDT, where Mol2 was a pyrazoloquinoline derivative called 1-phenyl-3-methyl-6-CF<sub>3</sub>-1*H*-pyrazolo[3,4-*b*]quinoline. Device 2, with the configuration ITO/PEDOT:PSS/Mol2 + PDT/Al, exhib-

ited power conversion efficiency of approximately 0.33%, with a short-circuit density of  $24.71 \mu\text{A}/\text{cm}^2$  and fill factor equal 0.21. The thickness of the active layers (Mol2 + PDT) was equal 105.6 nm.

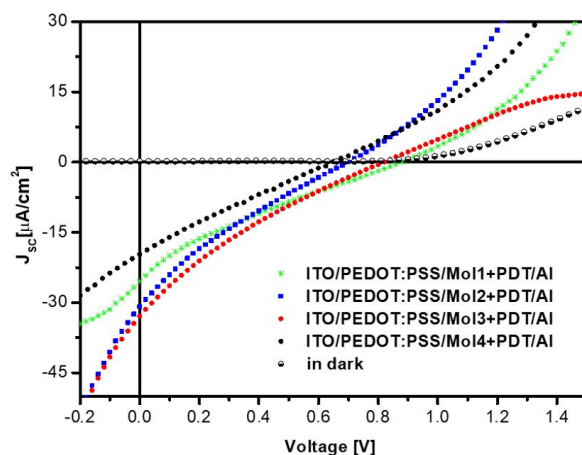


**Figure 11.** The dark and under illumination current density–voltage ( $J$ – $V$ ) characteristics of ITO/PEDOT:PSS/PDT + Mol $x$ /Al.

A comparable power efficiency 0.32 % was obtained for BHJ photovoltaic device 1, with structure of ITO/PEDOT:PSS/Mol1 + PDT/Al (Figure 11, Table 2), where the current density,  $J_{SC}$ , was  $30.88 \mu\text{A}/\text{cm}^2$  and the open-circuit voltage,  $V_{OC}$ , was approximately 0.7 V with a fill factor of 0.20. The thickness of the active layer (Mol1 + PDT) was equal to 102.9 nm (see Table 2). Photovoltaic device 4, based on Mol4 + PDT, exhibited a power conversion efficiency of approximately 0.21%. Molecule Mol4 (1,3-dimethyl-6-CF<sub>3</sub>-1*H*-pyrazolo[3,4-*b*]quinoline) was studied for its application in photovoltaic structures; the obtained results were presented at ICTON 2016 [71].

From the comparison of the thickness of the active layers and the efficiency of the photovoltaic cells, listed in Table 2, it can be seen that the greater thicknesses of the active layer correspond to greater efficiencies. However, the detailed optical analysis performed by us, based on the determined density distributions of the generated excitons, the absorption characteristics of Mol $x$  compounds and the spectral characteristics of the solar radiation simulator, showed that an increase in the thickness of the active layer should cause a decrease in efficiency. On the other hand, the factors causing the increase in efficiency are shifts in the absorption characteristics of individual compounds towards longer wavelengths. In the spectral range of the absorption of these compounds, the photon flux density of the simulator's radiation increases with the wavelength. Thus, the observed increase in efficiency is not an effect of increasingly thicker active layers but is an effect of the location of the absorption characteristics of individual compounds.

### 5.5. OLED Characterization

We also measured the electroluminescence spectra of prepared light-emitting diodes based on pyrazoloquinoline derivatives Mol $x$  ( $x = 1, 2, 3, 4$ )-doped PVK. These measurements were made using a Shimadzu UVVIS 2101 scanning spectrophotometer. OLEDs based on pyrazoloquinolines derivatives and polymer (PVK) exhibit strong electroluminescence emission with a spectra range of 481–506 nm.

The EL spectra of all fabricated organic blue-light emitting devices are shown in Figure 12. For OLED 1, with active layer (Mol1 + PVK), the bluish-green emission peak is at a wavelength of 489 nm (see Table 3), where Mol1 is the luminophore-doped PVK. This peak is spectrally shifted to a lower wavelength with respect to other luminophores. The electroluminescence (EL) spectrum of OLED 2, with active layer (Mol2 + PVK), and OLED 3, with (Mol3 + PVK), showed bluish-green emission maximum peaks,  $\lambda_{Elmax}$ , at wavelengths

492 nm and 506 nm, respectively, whereas OLED 4, with active layer (Mol4 + PVK), had an emission maximum peak,  $\lambda_{ELmax}$ , at 481 nm (see Table 3).

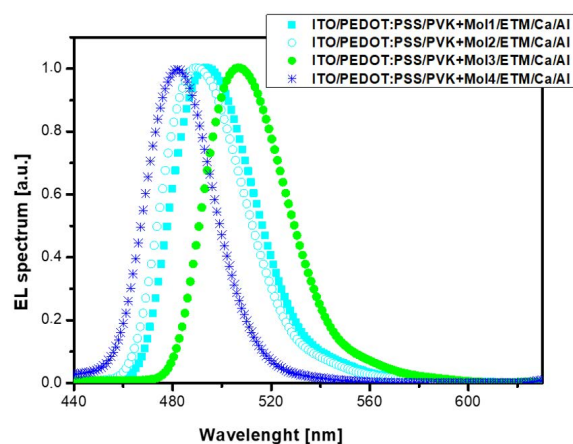


**Figure 12.** The normalized electroluminescence spectra emission of investigated OLEDs with configuration ITO/PEDOT:PSS/ETM/active layer/Ca/Al. Active layer was a blend of PVK and luminophore—Molx (where x = 1; 2; 3; 4). Additionally: (Mol1)—1-methyl-3-phenyl-6-CF<sub>3</sub>-1H-pyrazolo[3,4-*b*]quinoline; (Mol2)—1-phenyl-3-methyl-6-CF<sub>3</sub>-1H-pyrazolo[3,4-*b*]quinoline; (Mol3)—1-phenyl-3-phenyl-6-CF<sub>3</sub>-1H-pyrazolo[3,4-*b*]quinoline; (Mol4)—1-methyl-3-methyl-6-CF<sub>3</sub>-1H-pyrazolo[3,4-*b*]quinoline.

**Table 3.** Selected Properties of the Fabricated OLED Devices.

Molecule	$\lambda_{ELmax}$ (nm)	$U_T$ (V)	Brightness <sub>max</sub> (cd/m <sup>2</sup> )	Max CE (cd/A)	CIE <sub>xy</sub> Colour Coordinates
Mol1	493	8.66	1090.5	1.21	(0.032, 0.364)
Mol2	487	8.98	1030.6	1.10	(0.059, 0.235)
Mol3	506	10.32	1436.0	1.26	(0.007, 0.692)
Mol4	481	9.06	755.9	0.91	(0.087, 0.144)

We characterized the emission colour in the Commission International de l’Eclairage CIE-chromaticity (1931) using the EL spectra shown in Figure 12. The colour changes of the prepared double layer organic light emitting diodes are plotted in the CIE XYZ colour space (see (X,Y)-coordinates in Table 3, Z = 1 – X – Y) diagram, as presented in Figure 13. We can see that, for OLEDs based on 1-phenyl-3-phenyl-6-CF<sub>3</sub>-1H-pyrazolo[3,4-*b*]quinoline, the CIE colour-coordinates (x,y) are 0.032, 0.364 (see Table 3).

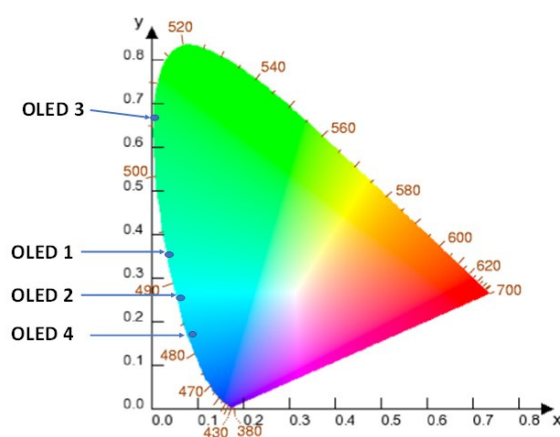


**Figure 13.** CIE colour-coordinates of prepared double-layer light emitting diodes (OLED 1, OLED 2, OLED 3, OLED 4).

Figures 14 and 15 show the luminance–voltage ( $L$ – $V$ ) and the current density–voltage ( $J$ – $V$ ) curves recorded for organic EL devices, respectively.

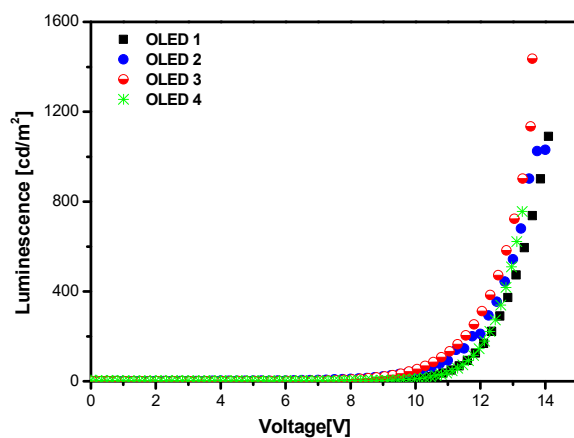


**Figure 14.** The luminance–voltage ( $L$ – $V$ ) curves for OLED1 with ITO/PEDOT:PSS/PVK + Mol1/ETM/Ca/Al; OLED2 with ITO/PEDOT:PSS/PVK + Mol2/ETM/Ca/Al; OLED3 with ITO/PEDOT:PSS/PVK + Mol3/ETM/Ca/Al; OLED4 with ITO/PEDOT:PSS/PVK + Mol4/ETM/Ca/Al.

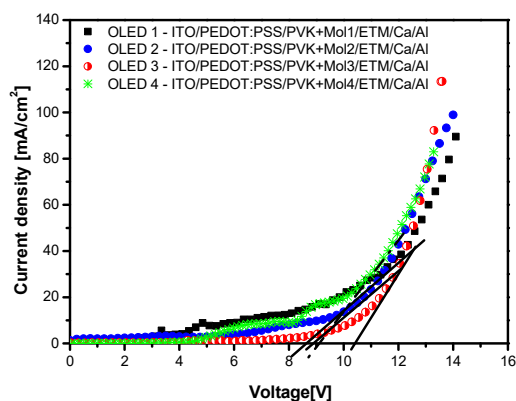


**Figure 15.** The current density–voltage curves for the prepared OLEDs ITO/PEDOT:PSS/PVK + luminophore/ETM/Ca/Al (luminophore Mol1, Mol2, Mol3, Mol4) configurations: Characteristics are labelled according to type of EL diodes active layer.

OLED 1, with the configuration ITO/PEDOT:PSS/active layer/ETM/Ca/Al, exhibited the maximal values of the brightness of approximately  $1090.5 \text{ cd/m}^2$ , with a current efficiency of  $1.21 \text{ cd/A}$  and CIE coordinates of  $0.032, 0.364$ . In this device, the active layer was a mixture of 1-methyl-3-phenyl-6- $\text{CF}_3$ -1*H*-pyrazolo[3,4-*b*]quinoline [ $\text{R}^1 = \text{Me}$ ,  $\text{R}^3 = \text{Ph}$  and  $\text{R}_6 = \text{CF}_3$ ] doped PVK. The best value of the maximum brightness around  $1436.0 \text{ cd/m}^2$  was achieved for device OLED 3 with configuration ITO/PEDOT:PSS/PVK + Mol3/ETM/Ca/Al. OLED 3 was based on 1-phenyl-3-phenyl-6- $\text{CF}_3$ -1*H*-pyrazolo[3,4-*b*]quinoline [ $\text{R}^1 = \text{Ph}$ ,  $\text{R}^3 = \text{Ph}$  and  $\text{R}_6 = \text{CF}_3$ ]. The current efficiency of the device based on Mol3 was up to  $1.26 \text{ cd/A}$ . As shown in Figure 14, a lower brightness  $S_{max}$  of approximately  $1030.6 \text{ cd/m}^2$  was received for OLED 2, with the structure ITO/PEDOT:PSS/PVK + Mol2/ETM/Ca/Al. In this double-layer architecture, the active layer was a blend of PVK and 1-phenyl-3-methyl-6- $\text{CF}_3$ -1*H*-pyrazolo[3,4-*b*]quinoline [ $\text{R}^1 = \text{Ph}$ ,  $\text{R}^3 = \text{Me}$  and  $\text{R}_6 = \text{CF}_3$ ]. OLED 2 showed current efficiencies of approximately  $1.10 \text{ cd/A}$ , with CIE coordinates of  $0.059, 0.235$ . For OLED 4, based on 1,3-dimethyl-6- $\text{CF}_3$ -1*H*-pyrazolo[3,4-*b*]quinoline [ $\text{R}^1 = \text{Me}$ ,  $\text{R}^3 = \text{Me}$  and  $\text{R}_6 = \text{CF}_3$ ], the maximal value of the brightness was approximately  $755.9 \text{ cd/m}^2$ , with CIE coordinates of  $0.087, 0.144$ .

The recorded current-density–voltage ( $J$ – $V$ ) characteristics for the prepared polymeric double layer EL diodes are shown in Figure 15. All  $J$ – $V$  curves presented complimentary

features and a typical character of obtained double layer OLEDs based on pyrazoloquinoline derivatives Molx (where x = 1, 2, 3, 4). The threshold voltages,  $U_T$ , designated as a result of measurement, are listed in the Table 3. All diodes showed a threshold voltage in the range of 8–10 V.

## 6. Conclusions

This paper presents synthesized pyrazoloquinoline derivatives and their physicochemical characterization. The photophysical studies showed that the photoinduced charge transfer phenomenon is responsible for energy deactivation of the first singlet excited state in the investigated phenyl-substituted pyrazoloquinolines. Our experiments revealed that phenyl at the 1st position plays a crucial role in the enhancement of charge transfer emission and in elevating the HOMO energy levels.

The produced compounds were used to produce active layers that were used in the structures of photovoltaic cells and OLEDs. For the produced photovoltaic cells, we obtained efficiencies below 0.4% and fill factors not exceeding 21%. Low efficiencies are primarily the result of too-high energy gaps of the compounds used and too-large thicknesses of the active layer. The developed compounds gave much better results in OLED diodes. We found a maximum brightness of 1436.0 (cd/m<sup>2</sup>) for OLED 3, based on 1*H*-pyrazolo [3,4-*b*] quinoline Mol3, with a maximum current efficiency of 1.26 cd/A. For all OLEDs, we obtained CIExy colour coordinates. These results demonstrate that 1*H*-pyrazolo[3,4-*b*]quinoline Mol3 is a promising host material for fluorescent dopants.

**Supplementary Materials:** The following supporting information can be downloaded at: <https://www.mdpi.com/article/10.3390/cryst12030434/s1>.

**Author Contributions:** Conceptualization: M.P.-K., E.G. and P.K.; photophysical/electrochemical/DFT characterization and calculations, T.U.; OLED/OPV device fabrication, E.G., M.P.-K. and K.W.; synthesis and characterization of molecules, A.D. and P.S.; methodology: M.P.-K., E.G., A.D., T.U., P.S. and K.W.; formal analysis: E.G. and P.K.; writing—original draft: M.P.-K., E.G., A.D. and T.U.; writing—review and editing, A.D., E.G. and M.P.-K. All authors have read and agreed to the published version of the manuscript.

**Funding:** This research received no external funding.

**Institutional Review Board Statement:** Not applicable.

**Informed Consent Statement:** Not applicable.

**Data Availability Statement:** Not applicable.

**Conflicts of Interest:** The authors declare no conflict of interest.

## References

1. Vogelbaum, H.S.; Sauve, G. Recently developed high-efficiency organic photoactive materials for printable photovoltaic cells: A mini review. *Synth. Met.* **2017**, *223*, 107–121. [[CrossRef](#)]
2. Paterson, A.F.; Singh, S.; Fallon, K.J.; Hodsden, T.; Han, Y.; Schroeder, B.C.; Bronstein, H.; Heeney, M.; McCulloch, I.; Anthopoulos, T.D. Recent Progress in High-Mobility Organic Transistors: A Reality Check. *Adv. Mater.* **2018**, *30*, 1801079. [[CrossRef](#)] [[PubMed](#)]
3. Lee, J.-H.; Chen, C.-H.; Lee, P.-H.; Lin, H.-Y.; Leung, M.-K.; Chiu, T.-L.; Lin, C.-F. Blue organic light-emitting diodes: Current status, challenges, and future outlook. *J. Mater. Chem. C* **2019**, *7*, 5874–5888. [[CrossRef](#)]
4. Semeniuk, M.; Yi, Z.; Poursorkhabi, V.; Tjong, J.; Jaffer, S.; Lu, Z.-H.; Sain, M. Future Perspectives and Review on Organic Carbon Dots in Electronic Applications. *ACS Nano* **2019**, *13*, 6224–6255. [[CrossRef](#)]
5. Kaur, G.; Adhikari, R.; Cass, P.; Bown, M.; Gunatillake, P. Electrically conductive polymers and composites for biomedical applications. *RSC Adv.* **2015**, *5*, 37553–37567. [[CrossRef](#)]
6. Zhu, M.; Meng, K.; Xu, C.; Zhang, J.; Ni, G. Lateral photovoltaic effect in ITO/PEDOT:PSS/MEH-PPV:PCBM/Al organic photovoltaic cells. *Org. Electron.* **2020**, *78*, 105585. [[CrossRef](#)]
7. Popoola, I.K.; Gondal, M.A.; Qahtan, T.F. Recent progress in flexible perovskite solar cells: Materials, mechanical tolerance and stability. *Renew. Sustain. Energy Rev.* **2018**, *82*, 3127–3151. [[CrossRef](#)]
8. Olalerua, S.A.; Kirui, J.K.; Wamwangi, D.; Roro, K.T.; Mwakikunga, B. Perovskite solar cells: The new epoch in photovoltaics. *Sol. Energy* **2020**, *196*, 295–309. [[CrossRef](#)]

9. Torabi, N.; Behjat, A.; Zhou, Y.; Docampo, P.; Stoddard, R.J.; Hillhouse, H.W.; Ameri, T. Progress and challenges in perovskite photovoltaics from single- to multi-junction cells. *Mater. Today Energy* **2019**, *12*, 70–94. [CrossRef]
10. Krebs, F.C. *Polymer Photovoltaics A Practical Approach*; Society of Photo-Optical Instrumentation Engineers (SPIE) Press: Bellingham, WA, USA, 2008.
11. Ganesamoorthy, R.; Sathiyam, G.; Sakthivel, P. Review: Fullerene based acceptors for efficient bulk heterojunction organic solar cell applications. *Sol. Energy Mater. Sol. Cells* **2017**, *161*, 102–148. [CrossRef]
12. Halls, J.J.M.; Arias, A.C.; MacKenzie, J.D.; Wu, W.; Inbasekaran, M.; Woo, E.P.; Friend, R.H. Photodiodes Based on Polyfluorene Composites: Influence of Morphology. *Adv. Mater.* **2000**, *12*, 498–502. [CrossRef]
13. Zhennan, G.; Jiuxin, Q.; Xihuang, Z.; Yongqing, W. Buckminsterfulleren C60: Synthesis, spectroscopic characterization and structure analysis. *J. Phys. Chem.* **1991**, *95*, 9615–9618. [CrossRef]
14. Krätschmer, W.; Lamb, L.D.; Fositropoulos, K.; Huffman, D.R. Solid C60: A new form of carbon. *Nature* **1990**, *347*, 354–358. [CrossRef]
15. Liu, Z.; Bao, C.; Xu, X.; Lei, G.; Gao, H.; Peng, Q.; Liu, Y. Tuning terminal units to improve the photovoltaic performance of small molecules based on a large planar fused ring core in solution-processed organic solar cells. *Org. Electron.* **2020**, *78*, 105566. [CrossRef]
16. Saunders, B.R.; Turner, M.L. Nanoparticle-polymer photovoltaic cells. *Adv. Colloid Interface Sci.* **2008**, *138*, 1–23. [CrossRef]
17. Sariciftci, N.S.; Smilowitz, L.; Heeger, A.J.; Wudl, F. Semiconducting polymers (as donors) and buckminsterfullerene (as acceptor): Photoinduced electron transfer and heterojunction devices. *Synth. Met.* **1993**, *59*, 333–352. [CrossRef]
18. Sariciftci, N.S.; Smilowitz, L.; Heeger, A.J.; Wudl, F. Photoinduced electron transfer from a conducting polymer to buckminsterfullerene. *Science* **1992**, *258*, 1474–1476. [CrossRef]
19. Yu, G.; Gao, J.; Hummelen, J.C.; Wudl, F.; Heeger, A.J. Polymer photovoltaic cells: Enhanced efficiencies via a network of internal donor-acceptor heterojunctions. *Science* **1995**, *270*, 1789–1791. [CrossRef]
20. Zhao, W.; Li, S.; Yao, H.; Zhang, S.; Zhang, Y.; Yang, B.; Hou, J. Molecular optimization enables over 13% efficiency in organic solar cells. *J. Am. Chem. Soc.* **2017**, *139*, 7148–7151. [CrossRef]
21. Yin, H.; Ho, J.K.W.; Cheung, S.H.; Yan, R.J.; Chiu, K.L.; Hao, X.; So, S.K. Designing a ternary photovoltaic cell for indoor light harvesting with a power conversion efficiency exceeding 20%. *J. Mater. Chem. A* **2018**, *6*, 8579–8585. [CrossRef]
22. Shittu, S.; Guiqiang, L.; Akhlaghi, Y.G.; Xiaoli, M.; Xudong, Z.; Ayodele, E. Advancements in thermoelectric generators for enhanced hybrid photovoltaic system performance. *Renew. Sust. Energ. Rev.* **2019**, *109*, 24–54. [CrossRef]
23. Benick, J.; Richter, A.; Müller, R.; Hauser, H.; Feldmann, F.; Krenkel, P.; Riepe, S.; Schindler, F.; Schubert, M.C.; Hermle, M.; et al. High efficiency n-type HP MC Silicon Solar Cells. *IEEE J. Photovolt.* **2017**, *7*, 1171–1175. [CrossRef]
24. Olindo, I.; Smets, A.H.M.; Zeman, M. Thin-film silicon—based quadrupole junction solar cells approaching 20% conversion efficiency. *Sol. Energy Mater. Sol. Cells* **2014**, *129*, 82–89. [CrossRef]
25. Kakiage, K.; Aoyama, Y.; Yano, T.; Oya, K.; Fujisawa, J.-I.; Hanaya, M. Highly-efficient dye-sensitized solar cells with collaborative sensitization by silyl-anchor and carboxy-anchor dyes. *Chem. Commun.* **2015**, *51*, 15894–15897. [CrossRef] [PubMed]
26. Chen, F.C. Emerging organic and organic/inorganic hybrid photovoltaic devices for specialty applications: Low level-lighting energy conversion and biochemical treatment. *Adv. Opt. Mater.* **2019**, *7*, 1800662. [CrossRef]
27. Helfrich, W.; Schneider, W.G. Recombination radiation in anthracene crystals. *Phys. Rev. Lett.* **1965**, *14*, 229. [CrossRef]
28. Tang, C.W.; VanSlyke, S.A. Organic electroluminescent diodes. *Appl. Phys. Lett.* **1987**, *51*, 913. [CrossRef]
29. Burroughes, J.H.; Bradley, D.D.C.; Brown, A.R.; Marks, R.N.; Mackay, K.; Friend, R.H.; Burns, P.L.; Holmes, A.B. Light emitting diodes based on conjugated polymers. *Nature* **1990**, *347*, 539–541. [CrossRef]
30. Zhao, X.; Wang, S.; You, J.; Zhang, Y.; Li, X. Solution-processed thermally stable amorphous films of small molecular hole injection/transport bi-functional materials and their application in high efficiency OLEDs. *J. Mater. Chem. C* **2015**, *3*, 11377–11384. [CrossRef]
31. Du, X.; Yang, X.; Zhao, J.; Lin, H.; Zheng, C.; Tao, S. Highly efficient solution-processed small molecule white organic light-emitting diodes. *Org. Electron.* **2016**, *38*, 344–349. [CrossRef]
32. Karzazi, Y. Organic light emitting diodes: Devices and applications. *J. Mater. Environ. Sci.* **2014**, *5*, 1–12. Available online: [https://www.jmaterenvironsci.com/Document/vol5/vol5\\_N1/1-JMES-607-2014-Karzazi.pdf](https://www.jmaterenvironsci.com/Document/vol5/vol5_N1/1-JMES-607-2014-Karzazi.pdf) (accessed on 16 March 2022).
33. Sandström, A.; Dam, H.F.; Krebs, F.C.; Edman, L. Ambient fabrication of flexible and large—Area organic light—Emitting devices using slot-die coating. *Nat. Commun.* **2012**, *3*, 1002. [CrossRef]
34. Karnakis, D.; Kearsley, A.; Knowles, M. Ultrafast laser patterning of OLEDs on flexible substrate for solid-state lighting. *J. Laser Micro Nanoeng.* **2009**, *4*, 218–223. [CrossRef]
35. Adachi, C.; Baldo, M.A.; Thompson, M.E.; Forrest, S.R. Nearly 100% internal phosphorescence efficiency in an organic light emitting device. *J. Appl. Phys.* **2001**, *90*, 5048–5051. [CrossRef]
36. Blom, P.W.M.; Berntsen, A.J.M.; Liednbaum, C.T.H.F.; Schoo, M.F.M.; Croonen, Y.; Van De Weijer, P. Efficiency and stability of polymer light-emitting diodes. *J. Mater. Sci. Mater. Electron.* **2000**, *11*, 105–109. [CrossRef]
37. Muccini, M.; Toffanin, S. *Organic Light-Emitting Transistors: Towards the Next Generation Display Technology*, 1st ed.; John Wiley & Sons: Hoboken, NJ, USA, 2016.
38. Xie, Z.Y.; Hung, L.S. High-contrast organic light-emitting diodes. *Appl. Phys. Lett.* **2004**, *84*, 1207. [CrossRef]

39. Ma, C.; Zhang, B.; Liang, Z.; Xie, P.; Wang, X.; Zhang, B.; Cao, Y.; Jiang, X.; Zhang, Z.J. A novel n-type red luminescent material for organic light-emitting diodes. *Mater. Chem.* **2002**, *12*, 1671–1675. [[CrossRef](#)]
40. Aizawa, N.; Pu, Y.-J.; Watanabe, M.; Chiba, T.; Ideta, K.; Toyota, N.; Igarashi, M.; Suzuri, Y.; Sasabe, H.; Kido, J. Solution processed multilayer small molecule light emitting devices with high efficiency white light emission. *Nat. Commun.* **2014**, *5*, 5756. [[CrossRef](#)]
41. Grykien, R.; Luszczynska, B.; Glowacki, I.; Kurach, E.; Rybakiewicz, R.; Kotwica, K.; Zagorska, M.; Pron, A.; Tassini, P.; Maglione, M.G.; et al. Photo- and electroluminescent properties of bithiophene disubstituted 1,3,4-thiadiazole and their application as active components in organic light emitting diodes. *Opt. Mater.* **2014**, *37*, 193–199. [[CrossRef](#)]
42. Shi, Z.; Zhang, X.; Wang, H.; Huo, J.; Zhao, H.; Shi, H.; Tang, B.Z. The synthesis, photoluminescence and electroluminescence properties of a new emitter based on diphenylethene, carbazole and 9,9,10,10-tetraoxidethianthrene. *Org. Electron.* **2019**, *70*, 7–13. [[CrossRef](#)]
43. Tao, Y.T.; Balasubramaniam, E.; Danel, A.; Jarosz, B.; Tomasik, P. Sharp green electroluminescence from 1H-pyrazolo[3,4-b]quinoline based light emitting diodes. *Appl. Phys. Lett.* **2000**, *77*, 1575. [[CrossRef](#)]
44. Tao, Y.T.; Chen, C.H.; Wu, F.I.; Shu, C.F.; Chien, C.H. SWpirobifluorene—Based pyrazoloquinolines: Efficient blue electroluminescent materials. *J. Mater. Chem.* **2004**, *14*, 1585–1589. [[CrossRef](#)]
45. Liu, C.; Li, Y.; Yang, C.; Wu, H.; Qin, J.; Cao, Y. Efficient solution—Processed deep blue organic light emitting diodes based on multibranch oligofluorenes with a phosphine oxide center. *Chem. Mater.* **2013**, *25*, 3320–3327. [[CrossRef](#)]
46. Kim, K.S.; Jeong, S.; Kim, C.; Ham, J.Y.; Kwon, Y.; Choi, B.D.; Han, Y.S. Synthesis and electro-optical properties of carbazole derivatives for organic device applications. *Synth. Met.* **2009**, *159*, 1870–1875. [[CrossRef](#)]
47. Brack, A. Über kondensierte Pyrazolopyridine. *Liebigs Ann. Chem.* **1965**, *681*, 105–110. [[CrossRef](#)]
48. Vilsmeier, A.; Haack, A. Über die Einwirkung von Halogenphosphor auf Alkyl-formanilide. Eine neue Methode zur Darstellung sekundärer und tertiärer p-Alkylamino-benzaldehyde. *Ber. Dtsch. Chem. Ges. A/B* **1927**, *60*, 119–122. [[CrossRef](#)]
49. Gondek, E. Optical optimization of organic solar cell with bulk heterojunction. *Opto-Electron. Rev.* **2014**, *22*, 77–85. [[CrossRef](#)]
50. Gondek, E. Optical optimization of organic solar cells. *Opt. Mater.* **2014**, *36*, 98–101. [[CrossRef](#)]
51. Gondek, E.P. Karasiński, High reflectance structures for photovoltaics applications—Analysis and characterization. *J. Mater. Sci. Mater. Electron.* **2013**, *24*, 2934–2943. [[CrossRef](#)]
52. Gondek, E.; Djaoued, Y.; Robichaud, J.; Karasiński, P.; Kityk, I.V.; Danel, A.; Pluciński, K.J. Influence of TiO<sub>2</sub> nanoparticles on the photovoltaic efficiency of the ITO/PEDOT:PSS/fluorine copolymers/polythiophene: TiO<sub>2</sub>/Al architecture. *J. Mater. Sci. Mater. Electron.* **2012**, *23*, 2057–2064. [[CrossRef](#)]
53. Gondek, E.; Kityk, I.V.; Danel, A. Molecular engineering by light emitting diode parameters on the base of methoxy-pyrazoloquinoline dyes in polysilane matrices. *J. Phys. D Appl. Phys.* **2007**, *40*, 2748–2753. [[CrossRef](#)]
54. Frisch, M.J.; Trucks, G.W.; Schlegel, H.B.; Scuseria, G.E.; Robb, M.A.; Cheeseman, J.R.; Scalmani, G.; Barone, V.; Petersson, G.A.; Nakatsuji, H.; et al. *Gaussian 16, Revision B.01*; Gaussian Inc.: Wallingford, CT, USA, 2016.
55. Brik, M.G.; Kuźnik, W.; Gondek, E.; Kityk, I.V.; Uchacz, T.; Szlachcic, P.; Jarosz, B.; Plucinski, K.J. Optical absorption measurements and quantum-chemical simulations of optical properties of novel fluoro derivatives of pyrazoloquinoline. *Chem. Phys.* **2010**, *370*, 194–200. [[CrossRef](#)]
56. Szlachcic, P.; Uchacz, T. Influence of fluorine on photophysical, electrochemical properties and basicity of 1,3-diphenylpyrazolo[3,4-b]quinoline derivatives. *J. Lumin.* **2018**, *194*, 579–587. [[CrossRef](#)]
57. Uchacz, T.; Szlachcic, P.; Danel, A.; Kukułka, M.; Srebro-Hooper, M.; Stopa, G.; Stadnicka, K.M. Photophysical properties of 1-pyridine-3-phenylpyrazoloquinoline and molecular logic gate implementation. *Dye. Pigment.* **2019**, *166*, 490–501. [[CrossRef](#)]
58. Becke, A.D. Density-functional thermochemistry. III. The role of exact exchange. *J. Chem. Phys.* **1993**, *98*, 5648. [[CrossRef](#)]
59. Lee, C.; Yang, W.; Parr, R.G. Development of the Colle-Salvetti correlation-energy formula into a functional of the electron density. *Phys. Rev. B* **1988**, *37*, 785–789. [[CrossRef](#)] [[PubMed](#)]
60. Stephens, P.J.; Devlin, F.J.; Chabalowski, C.F.; Frisch, M.J. Ab initio calculation of Vibrational Absorption and circular dichroism spectra using density functional force fields. *J. Phys. Chem.* **1994**, *98*, 11623–11627. [[CrossRef](#)]
61. Dunning, T.H., Jr. Gaussian basis sets for use in correlated molecular calculations. I. The atoms boron through neon and hydrogen. *J. Chem. Phys.* **1989**, *90*, 1007–1024. [[CrossRef](#)]
62. Tomasi, J.; Mennucci, B.; Cammi, R. Quantum mechanical continuum solvation models. *Chem. Rev.* **2005**, *105*, 2999–3094. [[CrossRef](#)]
63. Velapoldi, R.A. National Bureau of Standards Special Publication 378, Accuracy in Spectrophotometry and Luminescence Measurements. In Proceedings of the National Bureau of Standards, Gaithersburg, MD, USA, 22–24 March 1972; p. 231.
64. Montaser, A.A.; Abdel-Wahab, F. Spectroscopic ellipsometry investigations of Cd-Se thin film electrochemically prepared. *Optik* **2019**, *178*, 1270–1275. [[CrossRef](#)]
65. Uprety, P.; Junda, M.M.; Ghimire, K.; Adhikari, D.; Grice, C.; Podraza, N.J. Spectroscopic ellipsometry determination of optical and electrical properties of aluminium doped zinc oxide. *Appl. Surf. Sci.* **2017**, *421*, 852–858. [[CrossRef](#)]
66. Abdel-Wahab, F.; Merazga, A.; Rasheedy, M.S.; Montaser, A.A. Optical characterization of annealing effect on Ge<sub>5</sub>Te<sub>20</sub>Se<sub>75</sub> thin films by variable angle of-incidence spectroscopic ellipsometry. *Optik* **2016**, *127*, 3871–3877. [[CrossRef](#)]
67. Uchacz, T.; Szlachcic, P.; Wojtasik, K.; Mac, M.; Stadnicka, K. Amino derivatives of 1,3-diphenyl-1H-pyrazolo[3,4-b]quinoline—Photophysics and implementation of molecular switches. *Dye. Pigment.* **2016**, *124*, 277–292. [[CrossRef](#)]

68. D'Andrade, B.W.; Datta, S.; Forrest, S.R.; Djurovich, P.; Polikarpov, E.; Thomson, M.E. Relationship between the ionization and oxidation potentials of molecular organic semiconductors. *Org. Electron.* **2005**, *6*, 11–20. [[CrossRef](#)]
69. Thelakkat, M.; Schmidt, H.-W. Synthesis and properties of novel derivatives of 1,3,5-tris(diarylamino)benzenes for electroluminescent devices. *Adv. Mater.* **1998**, *10*, 219–223. [[CrossRef](#)]
70. Tauc, J.; Grigorovici, R.; Vancu, A. Optical properties and electronic structure of amorphous germanium. *Phys. Status Solidi B* **1966**, *15*, 627–637. [[CrossRef](#)]
71. Pokladko-Kowar, M.; Danel, A. Photovoltaic Cells Based on Organic Composites. In Proceedings of the 18th International Conference on Transparent Optical Networks, ICTON 2016, Trento, Italy, 10 July 2016; p. 7550270.